ARTICLE OPEN

Check for updates

Ultra-flexible semitransparent organic photovoltaics

Hanbee Lee[1,8], Soyeong Jeong[2,8], Jae-Hyun Kim[3,8], Yong-Ryun Jo[4], Hyeong Ju Eun[5], Byoungwook Park[6], Sung Cheol Yoon[6], Jong H. Kim[5]✉, Seung-Hoon Lee[7]✉ and Sungjun Park[1,3]✉

Ultra-flexible organic photovoltaics (OPVs) are promising candidates for next-generation power sources owing to their low weight, transparency, and flexibility. However, obtaining ultra-flexibility under extreme repetitive mechanical stress while maintaining optical transparency remains challenging because of the intrinsic brittleness of transparent electrodes. Here, we introduce strain-durable ultra-flexible semitransparent OPVs with a thickness below 2 μm. The conformal surface coverage of nanoscale thin metal electrodes (< 10 nm) is achieved, resulting in extremely low flexural rigidity and high strain durability. In-depth optical and electrical analyses on ultrathin metal electrodes showed that the devices maintain over 73% of their initial efficiency after 1000 cycles of repetitive compression and release at 66% compressive strain, and the average visible light transmittances remain higher than 30%. To our knowledge, this is the first systematical study on mechanical behaviors of strain-durable ultra-flexible ST-OPVs through precise adjustment of each ultrathin electrode thickness toward the emergence of next-generation flexible power sources.

npj Flexible Electronics (2023)7:27 ; https://doi.org/10.1038/s41528-023-00260-5

INTRODUCTION

Ultrathin (< 3 μm-thick) flexible organic photovoltaics (OPVs)[1–8] have attracted considerable attention owing to their inherent flexibility, low weight, and cost-effective large-area processibility. Although, the current power-conversion efficiency (PCE) of flexible OPVs is 17.52%, it is continuously increasing[1]. Several studies have focused on improving the environmental, operational, and mechanical stability of OPVs to facilitate practical integration in wearables[2,3] skin and tissue-compatible biomonitoring sensors[4,9–12], and Internet-of-Things devices[13,14] that do not require external power sources. Therefore, research on ultra-flexible OPVs has accelerated over the past decade[15–17].

In addition to the inherent mechanical softness of organic absorbers, the design and tailoring of molecular structures enable organic optoelectronic devices to be semitransparent (ST). Recent strategies for high visible transmittance include the optimization of the physical thickness and ratio of bulk heterojunction[18–20], introduction of wide-bandgap donor materials[21–23] and novel non-fullerene acceptor materials[24,25] for strong near-infrared absorption with the development of transparent top electrodes, such as Ag nanowires[1,26], graphene[27,28], conducting polymer[29,30], thin metals[18,31,32], and dielectric–metal–dielectric (DMD)[33–35]. The ST nature of these OPV devices enables their application to facades, rooftops, and windows for building- and greenhouse-integrated energy harvesting. Despite these desirable characteristics, the OPV performance is limited by the tradeoff between PCE and average visible transmittance (AVT). According to the survey on ST-OPVs summarized in Table S1, the highest PCE exceeds 15.2% with an AVT of 19.2% for rigid ST-OPVs[24], while the highest reported AVT is 82.0%, with a relatively low PCE of 0.43%[36]. Furthermore, the appropriate selection and engineering of transparent electrode materials are crucial for obtaining ST-OPVs with low flexural rigidity. Regarding flexibility benchmarks, most ultra-flexible OPVs have been demonstrated on ultrathin (~1 μm-thick) plastic substrates with rigid indium tin oxide (ITO) electrodes, exhibiting good mechanical durability against compression strain as high as 52% but poor performance retention under cycling tests (< 20 cycles)[6]. Alternatives to ITO electrodes, such as poly(3,4-ethylenedioxythiophene) polystyrene sulfonate (PEDOT:PSS)[37], Ag nanowires[38], and Ag meshes[8,39] have accomplished excellent stability under repetitive compression–release deformation over 1,000 cycles, but the compression strain has remained below 50%, and the electrodes were impenetrable. Recently, Liu[40] demonstrated ultra-flexible ST-OPV with a PCE of 4.06% and 2.38% when AVT is exceeding 70.0% and 80%, but a systematic study on the optical effect of electrodes and evaluation of mechanical stability under severe strain were not performed.

Developing ultra-flexible OPVs with transparency and mechanical durability remains challenging. The major difficulties arise because both a thick (~100 nm) top metal electrode with a high optical reflectivity and bottom ITO electrodes (~150 nm) with a high Young's modulus (> 100 GPa) are accommodated in the device on a soft polymeric substrate. In addition, neglecting the antireflective and mechanical properties of electrodes hinders achieving high transparency in visible wavelengths. Therefore, building thinner device architectures is required to achieve lower flexural rigidity considering both transparency and strain durability under repetitive and harsh deformations.

In this study, strain-durable ultra-flexible ST-OPVs were systematically investigated for the first time. An ultrathin Ag bottom electrode and a DMD top electrode were adopted to obtain devices with high transmittance and flexibility, and the highly efficient PTB7-Th:IEICO-4F was used as a photoactive material because it exhibits high PCE with low light absorption in visible light wavelengths (400–550 nm), contributing to optimize the transmittance of the photoactive layer. In addition, a polymer nucleation layer was employed to form a continuous thin metal film with thickness below the light penetration depth (<10 nm)

[1]Department of Electrical and Computer Engineering, Ajou University, Suwon 16499, Republic of Korea. [2]Department of Chemistry and Centre for Processable Electronics, Imperial College London, White City W12 0BZ, UK. [3]Department of Intelligence Semiconductor Engineering, Ajou University, Suwon 16499, Republic of Korea. [4]Advanced Photonics Research Institute (APRI), Gwangju Institute of Science and Technology (GIST), Gwangju 61005, Republic of Korea. [5]Division of Molecular Science and Technology, Ajou University, Suwon 16499, Republic of Korea. [6]Division of Advanced Materials, Korea Research Institute of Chemical Technology (KRICT), Daejeon 34114, Republic of Korea. [7]Division of Advanced materials Engineering, Kongju National University, 1223-24 Cheonan-daeroSeobuk-gu, Cheonan-si, Chungcheongnam-do, Republic of Korea. [8]These authors contributed equally: Hanbee Lee, Soyeong Jeong, Jae-Hyun Kim. ✉email: jonghkim@ajou.ac.kr; leesh23@kongju.ac.kr; sj0223park@ajou.ac.kr

and obtain highly conductive and transparent bottom electrodes[41]. An antireflection layer was introduced in the top DMD electrode to minimize light reflection and improve transmittance. To achieve high PCE with total device transparency, the absorption spectrum of the active material was analyzed based on the direction of the incident light, and the thickness of the bottom and top electrodes was optimized to maximize both AVT and PCE. Following the optimization of the optical and electrical properties of each film, an ultra-flexible ST-OPV with a thickness of only 2 μm was obtained, with highest PCE of 6.93 and AVT of 30.1% under different thickness of thin Ag layer, respectively. The ultra-flexible ST-OPVs exhibited excellent mechanical stability against strong biaxial tensile strain of approximately 200% and maintained over 73% of the initial PCE after 1,000 compression (tensile strain 0%)–release (tensile strain 200%). The findings of this study (Table S2) demonstrate the practical applicability of these ST-OPVs to biocompatible wearable devices.

RESULTS

Design of ultra-flexible ST-OPVs

Figure 1a, b show the device architecture and a photograph of the ultra-flexible ST-OPV developed in this study, respectively. The devices were fabricated on an ultrathin parylene/SU-8 substrate with an inverted structure comprising polyethyleneimine (PEI)/Ag/ZnO/photoactive layer/MoO_3/Ag/MoO_3; the corresponding energy levels are shown in Fig. S1. The total thickness of the device, including the substrate, was determined via cross-sectional transmission electron microscopy (TEM) to be approximately 2 μm (Fig. S2). An ultrathin Ag film (8 nm) was deposited as a transparent bottom electrode with a PEI/Ag/ZnO configuration, wherein PEI acted as a nucleation inducer for reducing the percolation threshold of the Ag layer through coordinative interaction between the amine group in PEI and Ag[41]. ZnO nanoparticles were used for the antireflection and electron-transport layer. To obtain an active light-absorbing layer (Fig. 1c), poly(4,8-bis(5-(2-ethylhexyl)thiophen-2-yl)benzo[1,2-b;4,5-b′] dithiophene-2,6-diylalt-(4-(2-ethylhexyl)-3 fluorothieno[3,4-b]thiophene-)-2-carboxylate-2-6-diyl (PTB7-Th) was used as donor and 2,2′-((2Z,2′Z)-(((4,4,9,9-tetrakis-(4-hexylphenyl)-4,9-dihydro-sindaceno[1,2-b:5,6-b′]-dithiophene-2,7-diyl)bis(4-((2-ethylhexyl)oxy) thiophene-5,2-diyl))bis(methanylylidene))bis(5,6-difluoro-3-oxo-2,3-dihydro-1H-indene-2,1-diylidene))dimalononitrile (IEICO-4F) was used as narrow-band gap acceptor[42] (E_g ~ 1.29 eV) owing to their strong absorption ability in the near-infrared region and high transmittance in the visible wavelength range. Subsequently, a DMD electrode comprising MoO_3/Ag/MoO_3 layers was deposited on the photoactive layer as a ST top electrode. Prior to evaluating

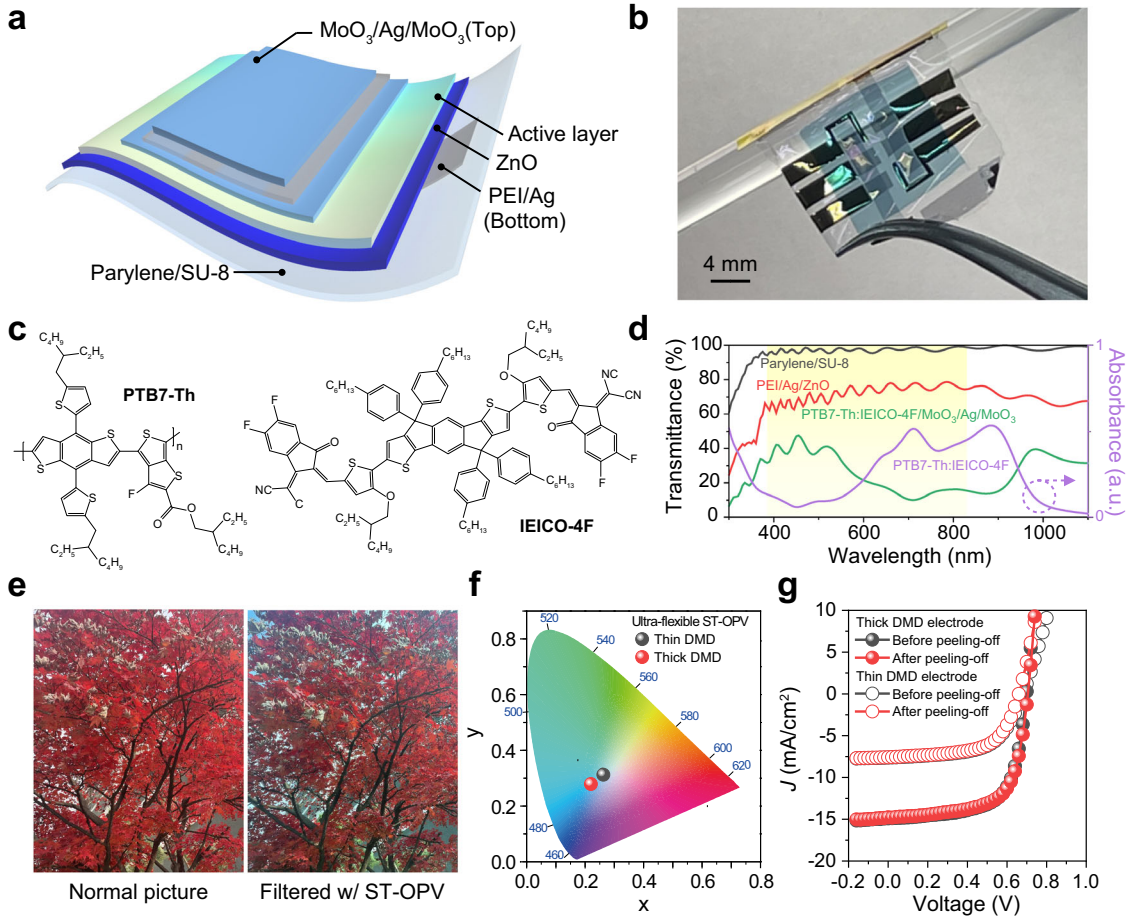

Fig. 1 Design of ultra-flexible ST-OPVs. a Schematic of the device structure and (**b**) a photograph of ultra-flexible ST-OPV. **c** Chemical structures of donor polymer, PTB7-Th, and non-fullerene acceptor, IEICO-4F. **d** Absorbance spectra of PTB7-Th:IEICO-4F film (purple) and transmittance spectra of glass/parylene/SU-8 (black), PEI/Ag/ZnO (red), PTB7-Th:IEICIO-4F/MoO3/Ag (8 nm)/ (green). **e** Images captured without obstruction (left) and through parylene (0.5 μm)/SU-8 (0.6 μm)/PEI/Ag (8 nm)/ZnO (50 nm)/PTB7-Th:IEICIO-4F (65 nm)/MoO_3 (5 nm)/Ag (8 nm)/MoO_3 (30 nm)/parylene (1 μm) (right). **f** Color coordinates of ST-OPVs with different thicknesses of DMD electrodes under standard D65 illumination in the CIE 1931 color space. **g** *J*–*V* characteristics of ultra-flexible ST-OPVs under solar illumination (1000 W/m^2) before and after peeling off from supporting glass. The detailed information regarding the thickness of the metal layer in the D/M/D structure and the transmittance of devices are shown in Fig. S3.

the device performance, ultraviolet–visible–near-infrared transmittance data of the layer-by-layer-deposited films were analyzed, as shown in Fig. 1d. As observed in the transmittance spectra, the fully deposited films of parylene/SU-8/PEI/Ag (8 nm)/ZnO nanoparticles/PTB7-Th:IEICO-4F/MoO_3 (5 nm)/Ag (8 nm)/MoO_3 (30 nm) exhibit relatively low transmission at approximately 650 and 840 nm in the spectrum owing to the presence of PTB7-Th:IEICO-4F in the light-absorbing layer. Furthermore, the PTB7-Th:IEICO-4F film exhibits relatively weak absorption in the 400–600 nm wavelength region, resulting in high transmittance of the ST device in the visible region. Figure 1e shows photographs captured without (left) and with (right) the ultra-flexible ST-OPV devices (2.4 × 2.4 cm, glass/parylene/SU-8/PEI/Ag (8 nm)/ZnO/PTB7-Th:IEICO-4F (62 nm)/MoO_3 (5 nm)/Ag (8 nm)/MoO_3 (30 nm)). An AVT of 30.1% was obtained, and the maple trees in the background could be clearly observed, indicating good transparency in the devices.

To compare the optical and electrical performance based on the reflection properties of top electrodes, the Ag layer thickness of the bottom electrode was fixed to 8 nm, whereas the top DMD electrodes were tested with Ag thicknesses of 25 and 8 nm. We note that 25 and 8 nm of Ag in DMD electrodes are chosen after careful optimization shown in Table S3 as representative conditions for the highest PCE and AVT, respectively. The AVT of the devices increased from 10.2% to 30.1% by decreasing the Ag layer thickness of the DMD electrode from 25 to 8 nm. Notably, the 380–600 nm region exhibited high transparency at different Ag layer thicknesses, which is a desirable characteristic for ST-OPVs (Fig. S3). However, when the Ag layer thickness was decreased, the CIE coordinates shifted toward the white color from (0.228, 0.279) to (0.267, 0.318), as shown in Fig. 1f. Ultra-flexible ST-OPVs with a thickness of 2 μm were obtained after the ST-OPV on the parylene/SU-8 substrate was carefully delaminated from the supporting glass (Fig. 1b). Figure 1g and S3 show the *J*–*V* characteristics and transmittance spectra of the ultra-flexible ST-OPVs with the two different DMD electrodes before and after delamination from the supporting glass, respectively. A clear tradeoff between the AVT and PCE was observed when the Ag layer thickness of the DMD electrode increased from 8 to 25 nm. The device with the 8 nm-thick Ag electrode exhibited a PCE of 3.09%, V_{oc} of 0.681 V, J_{sc} of 7.61 mA/cm^2, and FF of 59.8%, whereas the device with the 25 nm-thick Ag electrode exhibited a PCE of 6.91%, V_{oc} of 0.705 V, J_{sc} of 14.77 mA/cm^2, and FF of 66.3%. As summarized in Table 1, the performance of the devices remained unchanged after peel-off, indicating that the ultra-flexible ST-OPVs were fully functional even after being peeled off from the supporting glass. Low leakage current of the ST-OPV in the dark condition indicates minimal power losses in solar cells (Fig. S4). We also note that the AVT of the ultra-flexible ST-OPV was comparable to that of ST-OPVs on commercial ITO/glass substrates (see Fig. S5, S6 and Table S3). However, a trade-off between J_{sc} and FF was observed, which presumably comes from a higher reflection of the bottom Ag layer and lower R_{sheet} than that of ITO.

Electrical and optical properties of ultrathin electrodes

Our initial work on ultra-flexible ST-OPVs focused on the optimization of the top DMD electrodes and bottom PEI/Ag/ZnO electrode in the device structure (Fig. 2a). These electrodes are key components for enhancing the light absorption and antireflection properties. Several studies have employed the MoO_3/Ag/MoO_3 structure as a top DMD transparent electrode in ST devices owing to their good optical transparency[33–35]. In the DMD structure, the inner MoO_3 layer offers dual functionality as both a hole transport layer and a nucleation inducer for the thin Ag metal layer in the middle.

Controlling the thickness of the middle Ag and outer MoO_3 layers was important for reducing reflectance while maintaining high transmittance in fully fabricated devices. Notably, the outer MoO_3 layer could substantially reduce the reflectance of the Ag film owing to the difference in refractive indices between Ag and MoO_3 ($n \approx 2.1$)[33,34,43]. To evaluate the optical and electrical characteristics, DMD films were fabricated by varying the thickness of the middle Ag layer from 5 to 25 nm and that of the top MoO_3 layer from 0 to 30 nm (Fig. S7, S8).

In addition to the top electrodes, the optical and electrical characteristics of the PEI/Ag/ZnO bottom electrodes were studied. Ultrathin metal films with a thickness less than the penetration depth ($\leq$ 10 nm) have been considered good candidates for flexible transparent electrodes owing to their intrinsic flexibility and transparency. However, 3D metal island growth does not allow the metal film to form percolation pathways under the penetration depth[44]. For example, to form a neat Ag film on a flexible substrate with R_{sheet} of 10 ohm/sq, it needs to be deposited with a thickness over 15 nm[45]. To overcome this limit, we adopted PEI, which is considered a nucleation inducer. Compared with the neat Ag film, the percolation thickness of PEI (< 5 nm)/Ag can be notably reduced through the synergetic effect of an increase in surface energy at the PEI surface (Fig. S9) and a coordinative reaction between Ag and amine groups as metal nucleation inducer[41,45]. To minimize the reflection and improve the transmittance of the electrodes, ZnO nanoparticles were employed as an antireflection layer on the PEI/Ag films. By applying the same principle with the outer MoO_3 layer in the DMD electrode, the phase of the incident light could be shifted at the Ag/ZnO surface, and a destructive interference could be induced because the ZnO layer has a considerably higher refractive index ($n \approx 2.0$)[46] than the Ag film ($n \approx 0.3$)[45] in the visible range (Fig. 2a). We also investigated the Ag thin bottom electrodes by varying the thicknesses of Ag from 7 to 25 nm and ZnO layer from 35 to 50 nm (Fig. S10–S12).

The optical and electrical characteristics of the DMD and PEI/Ag/ZnO electrodes are shown in Fig. 2b–e. The top DMD films were optimized at the thicknesses of MoO_3 (5 nm)/Ag (8 nm)/MoO_3 (30 nm), and this was confirmed by the cross-sectional bright field-TEM and high-angle annular dark-field scanning TEM images (Fig. 2b and S2). As shown in Fig. 2d (and Fig. S8), R_{sheet} of the DMD electrodes drastically decreased from 1039 to 1.2 ohm/sq as the Ag thickness increased from 5 to 25 nm, whereas the highest AVT occurred at a thickness of 8 nm of Ag layer in DMD films. The DMD films with increased outer MoO_3 layer thicknesses (up to 30 nm) clearly exhibited more transparency (Fig. S7, S8 and Tables S4–S7). In Fig. 2e, the highest transmittance of DMD films in the visible region was obtained with the MoO_3 (5 nm)/Ag (8 nm)/MoO_3 (30 nm) structure, reaching an AVT of 78.6% with R_{sheet} of 13.0 ohm/sq. Meanwhile, the surface morphologies of the optimized PEI/Ag and PEI/Ag/ZnO films were investigated using scanning electron microscopy (SEM) images (Fig. 2c). The PEI/Ag film exhibited a smooth and continuous surface morphology, agreeing with the findings of previous studies[41,45]. From the SEM images shown in Fig. S13, we calculated the area ratio of the void density in films with 7, 8, and 9 nm-thick Ag layers. The corresponding area ratios were 7.5%, 0.3%, and 0.1%, respectively. This finding is consistent with previous reports on the voids reflecting light owing to light scattering at the void edges[44,47]. For the PEI/Ag/ZnO film, the film surface maintained continuity with a better-defined surface structure owing to ZnO, thus indicating that depositing ZnO does not affect the electrical characteristics of the PEI/Ag film (Fig. 2c and S11). As shown in Fig. 2d, e, R_{sheet} of the PEI/Ag/ZnO electrode decreased from 17 to 0.92 ohm/sq as the Ag thickness increased from 7 to 25 nm, while the highest AVT of the PEI/Ag/ZnO film occurred with the 8 nm-thick Ag layer and 50 nm-thick ZnO layer. The detailed optimization results are shown in Fig. S10–S12 and Tables S8–S10. Hence, the bottom Ag electrode could be successfully optimized with a PEI (5 nm)/Ag (8 nm)/ZnO (50 nm) structure showing a R_{sheet} of 7.58 ohm/sq and

Table 1. Device parameters and optical characteristics of ultra-flexible ST-OPVs based on PTB7-Th:IEICO-4F before and after peeling off.

Peel-off condition	Bottom electrode (Ag)	Top electrode (D/M/D)	V_{oc} (V)	J_{sc} (mA/cm^2)	FF (%)	PCE (%)	AVT (%)
Before	8 nm	5/8/30 nm	0.681	7.65	60.8	3.11	30.1
After			0.681	7.61	59.8	3.09	
Before	8 nm	5/25/30 nm	0.705	14.87	66.4	6.93	10.2
After			0.705	14.77	66.3	6.91	

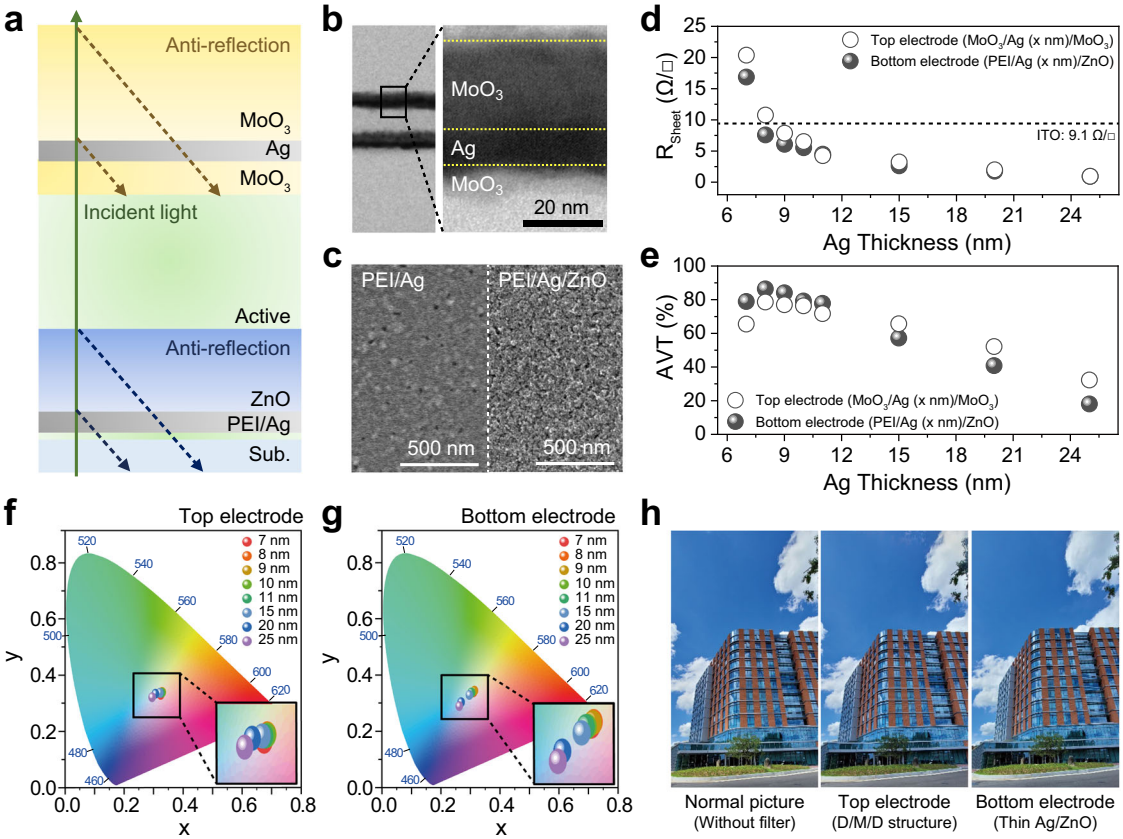

Fig. 2 Optical and electrical characteristics of ultrathin transparent electrodes. a Schematic of destructive interference in Ag films with antireflection layers. **b** Cross-sectional bright field-TEM image of top DMD film with thicknesses of 5, 8, and 30 nm. **c** SEM images of the PEI/Ag and PEI/Ag/ZnO films with 8 nm thickness. **d** Comparison of R_{sheet} according to Ag layer thickness in PEI/Ag/ZnO (5/x/50 nm) and DMD (5/x/30 nm) electrodes. **e** Comparison of AVTs according to Ag layer thickness in PEI/Ag/ZnO (5/x/50 nm) and DMD (5/x/30 nm). **e** Comparison of AVTs according to Ag layer thickness in PEI/Ag/ZnO and DMD electrodes. CIE coordinates of the (**f**) PEI/Ag/ZnO and (**g**) DMD electrodes with varying Ag layer thickness. **h** Photographs captured without filter (left), through DMD electrode (middle) and PEI/Ag/ZnO (right) electrode. The Ag layer thickness in the top and bottom electrodes was 8 nm.

the highest AVT of 86.4%. The low R_{sheet} values of DMD and PEI/Ag/ZnO electrodes were comparable to those of a commercial ITO electrode with lower flexural rigidity in terms of both conductivity and transparency.

To quantitatively evaluate the color of DMD and PEI/Ag/ZnO electrodes based on human visual perception, the CIE 1931 coordinates of both top and bottom electrodes were obtained as shown in Fig. 2f, g. The CIE coordinates of the electrodes in which Ag thickness was varied from 7 to 25 nm showed no notable difference, indicating suitable color neutrality close to that of the white color coordinates (0.330, 0.330), thus being favorable for application to windows. This is supported by the images shown in Fig. 2h, where buildings were photographed through the DMD electrode (middle) and PEI/Ag/ZnO electrode (right), showing transparency similar to that of a photograph captured without any filter (left).

Mechanical stability of ultrathin electrodes

To evaluate the mechanical flexibility of the transparent electrodes at the bottom and top, electrical tests were conducted on both parylene(0.5 μm)/SU-8(0.6 μm)/PEI(5 nm)/Ag(8 nm) and parylene (1 μm)/SU-8(500 nm)/DMD(5/8/30 nm) electrodes under mechanical deformation. Figure 3a shows a schematic of the lamination process of ultrathin electrodes on polymeric stretchable elastomers. First, the PEI/Ag and DMD electrodes were deposited on the glass/parylene/SU-8 substrate. For comparison, a 100 nm-thick ITO was fabricated onto the same substrate through sputtering[7,11]. Subsequently, the flexible transparent electrodes including parylene/SU-8 were peeled off from the supporting glass. Then, the flexible transparent electrodes were gently laminated on a 200% outward pre-stretched polymeric elastomer, which is pre-stretched to 3 times its initial size, i.e. 200% tensile strain. When the stretching force is reduced until the initial elastomer size, the

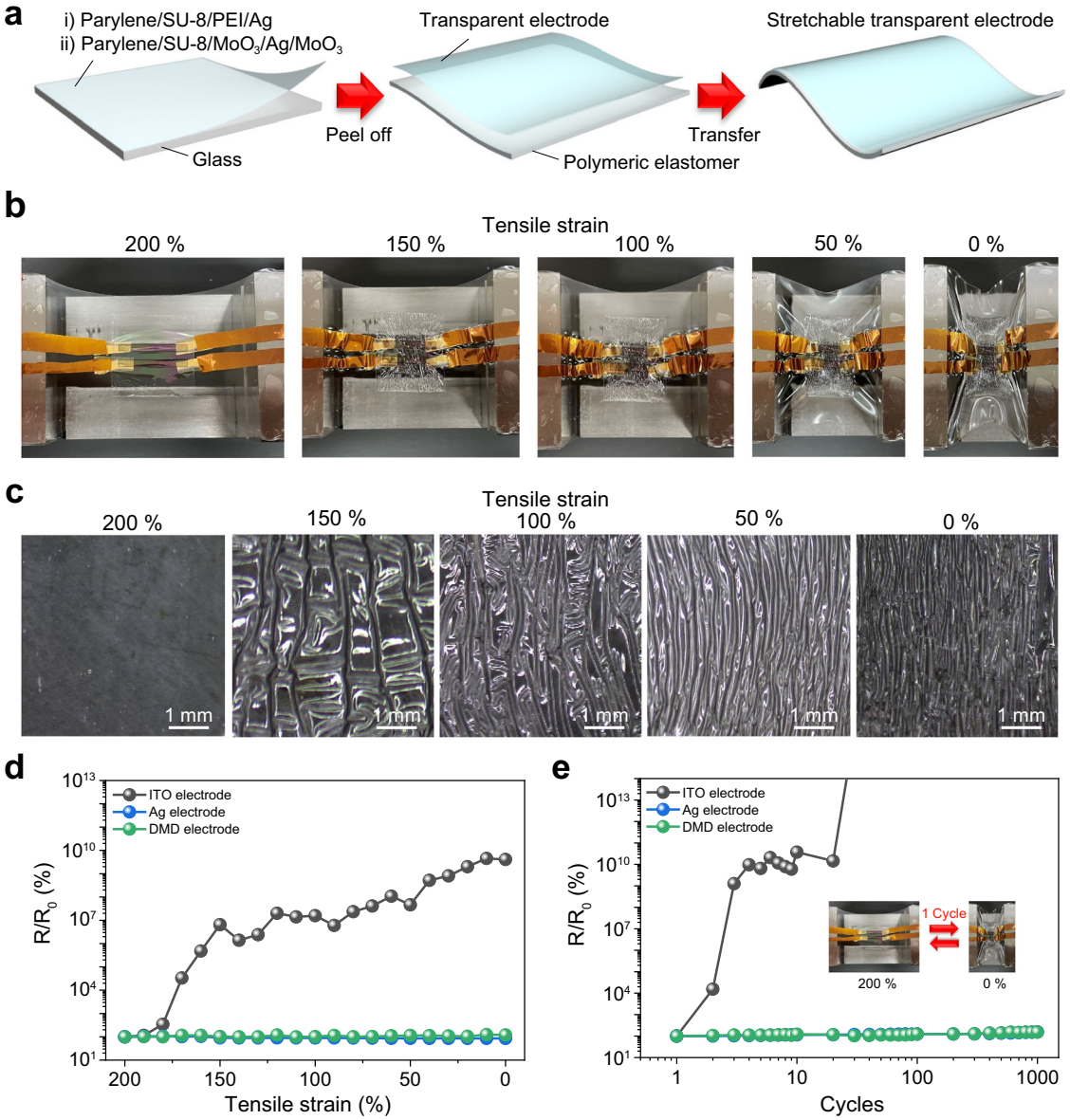

Fig. 3 Mechanical test of ultra-flexible transparent electrodes. a Schematic of fabrication of ultra-flexible transparent electrodes on parylene/SU-8 substrate. **b** Optical images of PEI/Ag electrodes from pre-stretched condition (200% tensile strain) to compressed condition (0% tensile strain) in tensile strain steps of 50%. **c** Images of ultrathin PEI/Ag electrodes laminated into polymeric elastomer from pre-stretched condition (200% tensile strain) to compressed condition (0% tensile strain) in tensile strain steps of 50%. Change in resistance in the ITO, PEI/Ag, and DMD electrodes (**d**), under a series of compression and (**e**), after repetitive cycles of compression–release.

tensile strain is reduced, i.e. 0% tensile strain. On the contrary, the compressive strain was applied from 0% to 66% to the elastomers by reducing the tensile strain from 200% to 0%, respectively. We note that 0% of tensile strain indicates that the pre-stretched elastomers recover to their initial size with 66% compressive strain.

Notably, the surfaces of flexible transparent electrodes became wrinkled as the tensile strain in the elastomer decreased toward 0% (Fig. 3b, c, and S14). Because the complex formation of wrinkles allowed biaxial compression, the R/R_0 values in the horizontal and vertical directions were measured during compression (forward) and release (backward) with 10% tensile strain steps. To obtain accurate R/R_0 values, patterned Cr/Au (10/100 nm) wirings were used as an electrical contact for the electrodes. As shown in Fig. 3d and S15, R/R_0 of the PEI/Ag and DMD electrodes maintained their initial values without notable changes along the horizontal and vertical directions, whereas R/R_0 of the ITO electrode increased drastically by 10^7 times the initial value and became unrecoverable owing to plastic deformation.

After repeating cycles of compression–release, no considerable performance degradation was observed in the PEI/Ag and DMD electrodes for up to 1,000 cycles, while the ITO electrode failed only after 20 cycles (Fig. 3e and S16). These results indicate that the percolation pathway of the Ag films in the electrodes can be maintained even under severe repetitive mechanical deformation, thus guaranteeing the mechanical stability of the PEI/Ag and DMD film electrodes. In addition to the electrical characterization under mechanical stress, the optical characteristics of the flexible bottom electrodes on an ultrathin substrate under different tensile strains were investigated. The highest AVTs of the flexible bottom and top electrodes with 8 nm-thick Ag layer were 68% and 64%, respectively, while the values of R_{sheet} before and after peeled off condition were 11.5 and 10.1 for thin Ag layer and those of before and after peeled off condition were 10.1 and 14.0 ohm/sq for thin

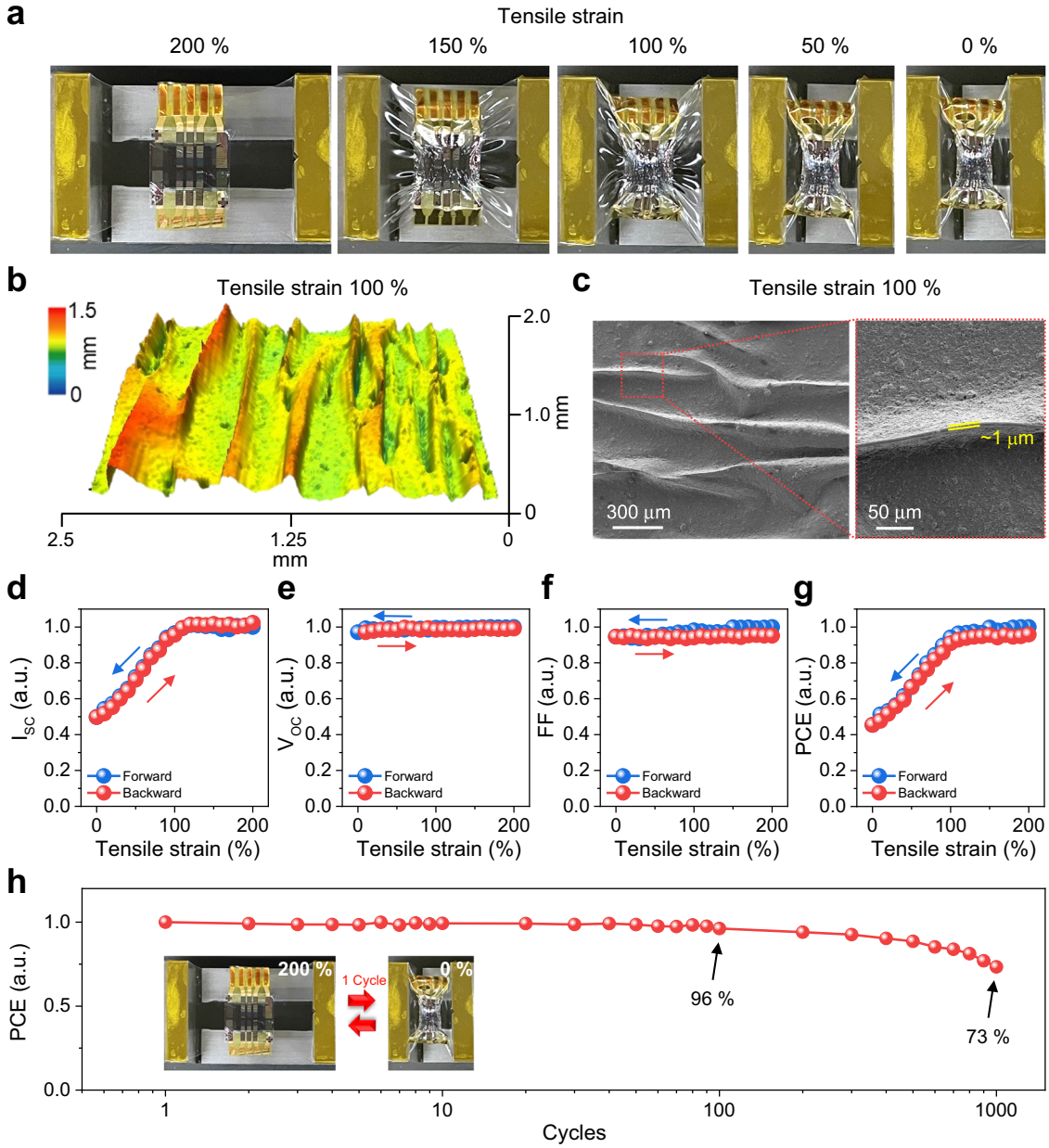

Fig. 4 Mechanical properties of ultra-flexible ST-OPVs. a Images of ultrathin ST-OPVs laminated into polymeric elastomer from pre-stretched condition (200% tensile strain) to compressed condition (0% tensile strain) with tensile strain steps of 50%. **b** 3D confocal microscope image of 100% tensile strained sample. **c** Top-view SEM image (left) of device surface at 100% tensile strain and enlarged image (right) indicating that bending radius below 1 μm. Changes in photovoltaic parameters of **d**, V_{OC}, **e** I_{SC}, **f** FF. **g** PCE under forward and backward compression. **h** Change in PCE of ST-OPVs under repetitive cycles of compression–release.

DMD layer, indicating negligible changes in resistivity during peeling off process, respectively (Fig. S17 and Tables S11–S12). Although the AVTs of the bottom and top electrodes decreased slightly owing to the wrinkles and folds when the tensile strain changed from 200% to 0%, they maintained 85% and 89% of their initial AVTs, respectively.

Strain-durable ultra-flexible ST-OPVs

Finally, inspired by the strain-durable and ultra-flexible top and bottom transparent electrodes, ultrathin ST-OPVs based on this device structure were fabricated and tested under mechanical deformation, as shown in Fig. 4a. To confirm the stability of the ultra-flexible ST-OPVs under extreme mechanical deformation, we transferred the delaminated ST-OPVs from the supporting glass to a pre-stretched polymeric elastomer. When the tensile strain in the polymeric elastomer was reduced from 200% to 0%, the devices compressed along the uniaxial direction and multiple wrinkles were induced (Fig. 4a). When the tensile strain was 100%, the SEM image of the compressed device showed multiple curvatures with bending radii below 1 μm. (Fig. 4b, c). To evaluate the performance changes of the ST-OPVs under compression, the *I*–*V* characteristics were measured every 10% tensile strain step. The corresponding device parameters are shown in Fig. 4d–g. The device remarkably maintained its initial performance during compression for 40 steps of continuous measurements. Only the I_{sc} values varied owing to the change in the effective absorption area of the devices, and no significant changes were observed in the V_{oc} and FF values. This implies that the nanoscale morphology

and charge extraction ability of the devices were maintained under extreme mechanical stress.

We also tested the mechanical stability of the ultra-flexible ST-OPV during 1000 cycles at 66% compressive strain. For comparison, we fabricated ITO-based ST-OPVs on parylene/SU-8 substrates. As shown in Fig. 4h and S18, all the device parameters of ITO-based ST-OPV decreased substantially compared with those from the first cycle and completely failed after 3 cycles, whereas those of the ultra-flexible ST-OPV maintained over 96% and 73% of the initial values until 100 and 1000 cycles, respectively.

Based on the results of this study, the ultrathin Ag electrodes seem promising for developing ITO-free transparent photovoltaic applications requiring transparency and ultra-flexibility, such as see-through skin-compatible and wearable power sources.

DISCUSSION

For future photovoltaic applications, the design of OPV structures with appealing aesthetics and ultra-flexibility will become more important. Our study has demonstrated that ultrathin Ag transparent electrodes are suitable candidates to improve the flexibility and appearance of OPVs. In this study, we demonstrated ultrathin and ultra-flexible ST-OPVs achieving a maximum PCE of 6.93% and AVT over 30% on a 1 μm-thick substrate under different thicknesses of thin Ag layer, respectively. To achieve both ultra-flexibility and transparency, an ultrathin PEI/Ag/ZnO bottom electrode and DMD top electrode were used. By varying the thicknesses of the Ag and antireflection layers in the transparent electrodes, the bottom electrode achieved AVT and R_{sheet} of 86.4% and 7.58 ohm/sq, respectively, while the top electrode achieved AVT and R_{sheet} of 78.6% and 13.0 ohm/sq, respectively. Both the top and bottom electrodes showed superior mechanical robustness against compressive strain because of the low flexural rigidity of the nanoscale-thickness metal electrodes. By using the PTB7-Th:IEICO-4F photoactive layer, the ST-OPVs fabricated on both glass and parylene/SU-8 substrates exhibited comparable PCE values without degradation. In addition to high optical and electrical performance, the ultra-flexible ST-OPVs showed high mechanical durability. The devices maintained 73% of the initial value after 1,000 compression (compressive strain 66%)–release (compressive strain 0%) cycles, while the ITO-based OPV failed after only 3 cycles. To the best of our knowledge, the extreme flexibility of the proposed ST-OPVs provides the highest reported performance, and they can pave the way for next-generation applications such as wearable skin-attached transparent power sources.

METHODS

Preparation of Materials

PTB7-Th (1-Materials) and IEICO-4F (Derthon) were used without further purification. The PTB7-Th:IEICO-4F mixed solution was prepared in chlorobenzene (99.8%, Sigma-Aldrich) with 4 vol% 1-chloronaphthalene ($C_{10}H_7Cl$, Sigma-Aldrich) at a total concentration of 20 mg/mL. PEI (Sigma-Aldrich, branched type 50% in H_2O) was dissolved in deionized water to form a 0.3 wt% aqueous solution. Amorphous ZnO nanoparticles were synthesized using the sol-gel method with zinc acetate dehydrate ($Zn(CH_3COO)_2{\cdot}2H_2O$). For elaboration, 2.97 g of zinc acetate dehydrate was dissolved in 125 mL of methanol and stirred at 60 °C. When the zinc acetate dehydrate was completely dissolved, a transparent solution was obtained. Then, 1.51 g of KOH dissolved in 65 mL of methanol at 60 °C was added to the transparent zinc acetate solution, and the mixed solution was then stirred at 60 °C for 3 h. The resultant cloudy solution was stored under ambient atmosphere for 4 h. After aging, the white precipitates in the solution were washed with methanol several times. The separated precipitates were redispersed in 12 mL of 1-butanol $(CH_3(CH2)_3OH)_5$ for ZnO dispersion. The as-prepared ZnO solution was transferred to a Teflon-lined autoclave for hydrothermal treatment at 170 °C for 1 h. After hydrothermal treatment, the solution turned milky white. Then, 2-(2-methoxyethoxy)acetic acid (MEAA-H) (4–6 wt%) was added to the prepared ZnO dispersed solution as a dispersion stabilizer, and the solution was shaken thoroughly. Finally, a bluish colloidal solution of crystalline ZnO nanoparticles was obtained. Before coating with this solution, the glass substrates were cleaned by sequential ultrasonication using detergent water, deionized water, acetone, and isopropanol for 5 min each. After ultrasonication, the cleaned substrates were blow-dried with nitrogen gas and O_2 plasma-treated at 100 W for 10 min (Femto Science) before deposition of the PEI solution. MoO_3 (100 mesh, 99.99%) and Ag (granule, 99.99%, iTASCO) electrodes were sequentially thermally evaporated with a customized thermal evaporator in a vacuum of 2.0×10^{-6} Torr.

Electrode and device fabrication

To prepare the ultra-flexible substrate, glass substrates were sequentially cleaned with detergent, deionized water, acetone, and isopropyl alcohol for 5 min each via ultrasonic treatment and blow-dried with nitrogen gas. To remove the residual chemicals on top of the glass surface, O_2 plasma treatment was applied for 10 min after cleaning. A fluorinated polymer blended solution (Novec 1700:7100, 1:10 vol%, 3M™) was spin-coated onto the cleaned glass substrate at 2000 rpm for 60 s, and a 0.5 μm-thick parylene film was deposited onto the surface of the fluorinated polymer/glass substrate through chemical vapor deposition. After the deposition of the parylene layer, the substrates were thermally annealed in an ambient atmosphere at 150 °C for 1 h. Subsequently, a 600 nm-thick epoxy (SU-8 3005, MicroChem) layer was spin-coated (5000 rpm for 60 s) for surface planarization. After exposing the film to ultraviolet light ($\lambda \approx 365$ nm) for 4 min, it was annealed at 95 °C for 2.5 min and then annealed in a nitrogen atmosphere at 150 °C for 1 h. The bottom electrodes were fabricated in two ways. 1) A 100 nm-thick ITO layer was sputtered without substrate heating and patterned using a photolithography process and wet etching. 2) An 8 nm-thick Ag layer was thermally deposited by a thermal evaporator at a deposition rate of 1.0 Å/s under vacuum pressure below 2.0×10^{-6} Torr. Before Ag deposition, the prepared aqueous PEI solution was dip-coated on the prepared substrate after surface treatment with O_2 plasma (100 W for 10 min). A 50 nm-thick layer of ZnO nanoparticles was spin-coated at 2000 rpm for 40 s. The mixed solution of the active layer materials, namely, PTB7-Th:IEICO-4F, was deposited in a argon glove box at 3000 rpm for 30 s. MoO_3 (5 nm) and Ag (8, 15, 20, 25 nm; as a top electrode) layers were sequentially deposited by a thermal evaporator under vacuum ($< 2.0 \times 10^{-6}$ Torr). To complete and form a passivation layer, a 1 μm-thick parylene film was deposited by chemical vapor deposition. Before measurements, the freestanding ultra-flexible organic solar cells were laminated onto a pre-stretched acrylic elastomer substrate (VHB Y-4905J, 3 M).

Mechanical property measurements

To record accurate electrical signals, gold external wirings were used as the electrical contacts of the freestanding devices. The gold wirings were fabricated by depositing patterned Cr/Au layers (10/100 nm) on 12.5 μm-thick polyimide films through a shadow mask. Contacts between the devices and gold wirings were established using electrically conductive adhesive tape (ECATT 9703, 3 M). The edges of the gold wirings were connected using alligator clips. Stretching was controlled using an in-house stretching screw machine with a ruler, and the measurements were taken under ambient conditions. Electrical data during the stretching test were recorded using a Keithley 2400 source meter.

Characterization

The current–voltage (*I*–*V*) characteristics were recorded at AM 1.5 G (100 mW/cm^2 with the intensity calibrated using a silicon reference diode (BS-520BK) using an XES-50S2 solar simulator (San-Ei, Japan) and Keithley 2400 source meter (Tektronix, USA) under ambient conditions. A typical cell device area of 0.04 cm^2 was defined using a metal shadow mask. The transmittances of films in the visible range were acquired using a V-770 ultraviolet/visible/near-infrared spectrophotometer (Jasco, Japan). For the measurement setup, the laminated films on the polymeric layer were fixed and located with film holder (FLH-740), and the percentile of compression was measured by checking the distance of indicators at both edge side marked on elastomers. The distance of indicators is 6 cm for 200% of tensile strain and 3 cm for 100 % of tensile strain, respectively. The transmittance data were measured by subtraction of those of reference samples. The transmittance data of the devices were measured by subtracting the transmittance values of the glass samples placed in the reference beam. This subtraction aimed to eliminate the influence of the supporting glass substrate used for the measurement, particularly for ultra-flexible devices. A comparison of the calculated AVT values derived from the transmittance data using both glass substrate and air as references are depicted in Fig. S19 and summarized in Supplementary Table 13. Contents related to AVT and CIE calculations are provided in the supporting information. The SEM images were obtained using a JSM-7900F microscope (Jeol, USA) operated at 15 kV. For the measurement, the devices on polymeric elastomers with 50% of compressive strain were loaded in the chamber. Bright field-TEM images, high-angle annular dark-field scanning TEM images, and energy-dispersive X-ray spectroscopy (EDS) spectrum were examined using a Tecnai G2 F30 S-Twin microscope operated at 300 kV. The confocal images were obtained using an OLS3000-300 mm auto-stage microscope. Origin software was used to perform the analyses and obtain the plots.

Reporting summary

Further information on research design is available in the Nature Research Reporting Summary linked to this article.

DATA AVAILABILITY

The data that support the plots within this paper and other findings of this study are available from the corresponding author upon reasonable request.

Received: 4 December 2022; Accepted: 19 May 2023;
Published online: 03 June 2023

REFERENCES

1. Zeng, G. et al. Realizing 17.5% Efficiency flexible organic solar cells via atomic-level chemical welding of silver nanowire electrodes. *J. Am. Chem. Soc.* **144**, 8658–8668 (2022).
2. Arumugam, S. et al. Fully spray-coated organic solar cells on woven polyester cotton fabrics for wearable energy harvesting applications. *J. Mater. Chem. A* **4**, 5561–5568 (2016).
3. Hashemi, S. A., Ramakrishna, S. & Aberle, A. G. Recent progress in flexible–wearable solar cells for self-powered electronic devices. *Energy Environ. Sci.* **13**, 685–743 (2020).
4. Savagatrup, S. et al. Plasticization of PEDOT:PSS by common additives for mechanically robust organic solar cells and wearable sensors. *Adv. Funct. Mater.* **25**, 427–436 (2015).
5. Kaltenbrunner, M. et al. Ultrathin and lightweight organic solar cells with high flexibility. *Nat. Commun.* **3**, 770 (2012).
6. Jinno, H. et al. Stretchable and waterproof elastomer-coated organic photovoltaics for washable electronic textile applications. *Nat. Energy* **2**, 780–785 (2017).
7. Park, S. et al. Self-powered ultra-flexible electronics via nano-grating-patterned organic photovoltaics. *Nature* **561**, 516–521 (2018).
8. Jiang, Z. et al. Durable ultraflexible organic photovoltaics with novel metal-oxide-free cathode. *Adv. Funct. Mater.* **29**, 1808378 (2019).
9. Choi, J. et al. Wearable self-powered pressure sensor by integration of piezo-transmittance microporous elastomer with organic solar cell. *Nano Energy* **74**, 104749 (2020).
10. Chow, P. C. Y. & Someya, T. Organic photodetectors for next-generation wearable electronics. *Adv. Mater.* **32**, 1902045 (2020).
11. Park, S. et al. Ultraflexible near-infrared organic photodetectors for conformal photoplethysmogram sensors. *Adv. Mater.* **30**, 1802359 (2018).
12. Kan, B., Ershad, F., Rao, Z. & Yu, C. Flexible organic solar cells for biomedical devices. *Nano Res.* **14**, 2891–2903 (2021).
13. Fukuda, K., Yu, K. & Someya, T. The future of flexible organic solar cells. *Adv. Energy Mater.* **10**, 2000765 (2020).
14. Ma, L.-K. et al. High-efficiency indoor organic photovoltaics with a band-aligned interlayer. *Joule* **4**, 1486–1500 (2020).
15. Huang, W. et al. Efficient and mechanically robust ultraflexible organic solar cells based on mixed acceptors. *Joule* **4**, 128–141 (2020).
16. Sun, Y. et al. Flexible organic photovoltaics based on water-processed silver nanowire electrodes. *Nat. Electron.* **2**, 513–520 (2019).
17. Zheng, X. et al. High-efficiency ITO-free organic photovoltaics with superior flexibility and upscalability. *Adv. Mater.* **34**, 2200044 (2022).
18. Hu, Z. et al. Semitransparent ternary nonfullerene polymer solar cells exhibiting 9.40% efficiency and 24.6% average visible transmittance. *Nano Energy* **55**, 424–432 (2019).
19. Song, Y. et al. Semitransparent organic solar cells enabled by a sequentially deposited bilayer structure. *ACS Appl. Mater. Interfaces* **12**, 18473–18481 (2020).
20. Schopp, N. et al. Unraveling device physics of dilute-donor narrow-bandgap organic solar cells with highly transparent active layers. *Adv. Mater.* **34**, 2203796 (2022).
21. Chen, K.-S. et al. Semi-transparent polymer solar cells with 6% PCE, 25% average visible transmittance and a color rendering index close to 100 for power generating window applications. *Energy Environ. Sci.* **5**, 9551–9557 (2012).
22. Liu, Y. et al. Enhancing the performance of non-fullerene organic solar cells using regioregular wide-bandgap polymers. *Macromolecules* **51**, 8646–8651 (2018).
23. Su, W. et al. Efficient as-cast semi-transparent organic solar cells with efficiency over 9% and a high average visible transmittance of 27.6%. *Phys. Chem. Chem. Phys.* **21**, 10660–10666 (2019).
24. Jing, J. et al. Semitransparent organic solar cells with efficiency surpassing 15%. *Adv. Energy Mater.* **12**, 2200453 (2022).
25. Cheng, H.-W., Zhao, Y. & Yang, Y. Toward high-performance semitransparent organic photovoltaics with narrow-bandgap donors and non-fullerene acceptors. *Adv. Energy Mater.* **12**, 2102908 (2022).
26. Lu, H. et al. Inkjet printed silver nanowire network as top electrode for semi-transparent organic photovoltaic devices. *Appl. Phys. Lett.* **106**, 093302 (2015).
27. Song, Y., Chang, S., Gradecak, S. & Kong, J. Visibly-transparent organic solar cells on flexible substrates with all-graphene electrodes. *Adv. d. Energy Mater.* **6**, 1600847 (2016).
28. Liu, Z., Li, J. & Yan, F. Package-free flexible organic solar cells with graphene top electrodes. *Adv. Mater.* **25**, 4296–4301 (2013).
29. Fan, X. et al. Highly conductive stretchable all-plastic electrodes using a novel dipping-embedded transfer method for high-performance wearable sensors and semitransparent organic solar cells. *Adv. Electron. Mater.* **3**, 1600471 (2017).
30. Zhang, Y. et al. Colorful semitransparent polymer solar cells employing a bottom periodic one-dimensional photonic crystal and a top conductive PEDOT:PSS layer. *J. Mater. Chem. A* **4**, 11821–11828 (2016).
31. Liu, Y. et al. Unraveling sunlight by transparent organic semiconductors toward photovoltaic and photosynthesis. *ACS Nano* **13**, 1071–1077 (2019).
32. Xu, G. et al. High-performance colorful semitransparent polymer solar cells with ultrathin hybrid-metal electrodes and fine-tuned dielectric mirrors. *Adv. Funct. Mater.* **27**, 1605908 (2017).
33. Çetinkaya, Ç. et al. Design and fabrication of a semi-transparent solar cell considering the effect of the layer thickness of MoO_3/Ag/MoO_3 transparent top contact on optical and electrical properties. *Sci. Rep.* **11**, 13079 (2021).
34. Lee, J. et al. Toward visibly transparent organic photovoltaic cells based on a near-infrared harvesting bulk heterojunction blend. *ACS Appl. Mater. Interfaces* **12**, 32764–32770 (2020).
35. Sun, G. et al. Highly-efficient semi-transparent organic solar cells utilising non-fullerene acceptors with optimised multilayer MoO_3/Ag/MoO_3 electrodes. *Mater. Chem. Front.* **3**, 450–455 (2019).
36. Ball, M. L. et al. Design of UV-absorbing donor molecules for nearly imperceptible organic solar cells. *ACS Energy Lett.* **7**, 180–188 (2022).
37. Song, W. et al. Crumple durable ultraflexible organic solar cells with an excellent power-per-weight performance. *Adv. Funct. Mater.* **31**, 2102694 (2021).
38. Qin, F. et al. Robust metal ion-chelated polymer interfacial layer for ultraflexible non-fullerene organic solar cells. *Nat. Commun.* **11**, 4508 (2020).

39. Jiang, Z. et al. Reverse-offset printed ultrathin ag mesh for robust conformal transparent electrodes for high-performance organic photovoltaics. *Adv. Mater.* **30**, 1707526 (2018).
40. Meng, R., Jiang, Q. & Liu, D. Balancing efficiency and transparency in organic transparent photovoltaics. *npj Flex. Electron.* **6**, 39 (2022).
41. Kang, H., Jung, S., Jeong, S., Kim, G. & Lee, K. Polymer-metal hybrid transparent electrodes for flexible electronics. *Nat. e Commun.* **6**, 6503 (2015).
42. Yao, H. et al. Design, synthesis, and photovoltaic characterization of a small molecular acceptor with an ultra-narrow band gap. *Angew. Chem., Int. Ed. Engl.* **56**, 3045–3049 (2017).
43. Upama, M. B. et al. High performance semitransparent organic solar cells with 5% PCE using non-patterned MoO_3/Ag/MoO_3 anode. *Curr. Appl. Phys.* **17**, 298–305 (2017).
44. Sennett, R. S. & Scott, G. D. The structure of evaporated metal films and their optical properties. *J. Opt. Soc. Am.* **40**, 203–211 (1950).
45. Jeong, S. et al. Role of polymeric metal nucleation inducers in fabricating large-area, flexible, and transparent electrodes for printable electronics. *Adv. Funct. Mater.* **27**, 1606842 (2017).
46. de Menezes, L. R., Cavalcante, M. D. P., Vaz, J. D. L. M. R., Silva, P. S. R. C. D. & Tavares, M. I. B. Obtention of higher refractive index and transparent polymeric nanocomposite systems with small amounts of fillers for lenses application. *J. Compos. Mater.* **55**, 675–686 (2021).
47. Zou, J., Li, C.-Z., Chang, C.-Y., Yip, H.-L. & Jen, A. K.-Y. Interfacial engineering of ultrathin metal film transparent electrode for flexible organic photovoltaic cells. *Adv. Mater.* **26**, 3618–3623 (2014).

ACKNOWLEDGEMENTS

This work was supported by the National Research Foundation of Korea(NRF) grant funded by the Korea government(MSIT) (No. RS-2023-00213089). This work was supported by the Technology Innovation Program (Grant No. RS-2022-00154781, Development of large-area wafer-level flexible/stretchable hybrid sensor platform technology for form factor-free highly integrated convergence sensor) funded by the Ministry of Trade, Industry & Energy (MOTIE, Korea). This research was also supported by the MSIT, Korea, under the ITRC (Information Technology Research Center) support program (Grant No. IITP-2023-2020-0-01461) supervised by the IITP (Institute for Information & communications Technology Planning & Evaluation). This study was supported by the National Research Foundation of Korea (NRF) funded by the Ministry of Science and ICT (NRF-2021K1A4A7A03093851).

AUTHOR CONTRIBUTIONS

S.P. conceived the idea and supervised the project. H.L., S.J., and J.H.K., who are co-first authors in this paper, fabricated the ultra-thin metal electrodes and characterized electrical properties under mechanical deformation. H.L. and J.H.K. fabricated flexible solar cells and measured electrical and optical properties. Y.R.J. analyzed the cross-sectional bright field-TEM and high-angle annular dark-field scanning TEM data. H.J.E., B.P., and S.C.Y. analyzed most of the data. J.H.K., S.-H.L., S.J., and S.P. wrote the manuscript. All authors discussed and commented on the manuscript.

COMPETING INTERESTS

The authors declare no competing interests.

ADDITIONAL INFORMATION

Supplementary information The online version contains supplementary material available at https://doi.org/10.1038/s41528-023-00260-5.

Correspondence and requests for materials should be addressed to Jong H. Kim, Seung-Hoon Lee or Sungjun Park.

Reprints and permission information is available at http://www.nature.com/reprints

Publisher's note Springer Nature remains neutral with regard to jurisdictional claims in published maps and institutional affiliations.